lubricants

MDPI

Article

Research on Rotor Dynamic Characteristics of High Speed Aviation Piston Pump

Lijun Chen [1,2,3], Rushen Deng [4], Jun Zha [5,*], Jianning Gu [1,2,3], Tianxiang Xia [1,2,3,*] and Runlin Chen [4]

[1] The State Key Laboratory of Fluid Power Components & Mechatronic Systems, School of Mechanical Engineering, Zhejiang University, Hangzhou 310027, China; clj@avic.com (L.C.)
[2] AVIC Nanjing Engineering Institute of Aircraft Systems, Nanjing 211102, China
[3] Aviation Key Laboratory of Science and Technology on Aero Electromechanical System Integration, Nanjing 211102, China
[4] School of Mechanical and Precision Instrument Engineering, Xi'an University of Technology, Xi'an 710048, China
[5] School of Mechanical Engineering, Xi'an Jiaotong University, Xi'an 710049, China
* Correspondence: jun_zha@xjtu.edu.cn (J.Z.); xiatx001@avic.com (T.X.); Tel.: +86-18392186598 (J.Z.); +86-13809009646 (T.X.)

Abstract: The high-speed aviation piston pump plays a vital role in hydraulic systems in the aviation field. Extremely complex force situations happen during running operations due to the coupling between multiple components, as a result of the overall dynamic characteristics being complex and changeable, which brings great difficulties and challenges to its performance optimization. Taking the high-speed aviation piston pump as the research object, a mechanical balance equation of the piston based on the dynamic balance method was proposed. The reaction force of the swashplate and the influence of rotational speed and outlet pressure on it were modeled. Through the balance of the system and the component subsystem, the load of the support bearing of the piston pump under different working conditions is analyzed, as well as the influence of the rotational speed and the outlet pressure on the bearing stiffness by the quasi-static method. In addition, the discrete model of the piston pump spindle and the discrete model of the rotor system are established. The accuracy of the model is verified by the finite element method. The maximum error of the spindle discrete model is 6.13%, and the maximum error of the rotor system discrete model is 15.28%. The transfer matrix analysis shows that the working condition parameters have little effect on the critical speed of the spindle and rotor system, and the outlet pressure has a more significant effect than the speed. The research results provide a theoretical basis and analysis method for the dynamic analysis and structural optimization of the high-speed aviation piston pump.

Keywords: piston pump; bearing rotor system; dynamic characteristics; critical speed; bearing stiffness; modal shape

check for updates

Received: 18 December 2024
Revised: 15 January 2025
Accepted: 23 January 2025
Published: 25 January 2025

Citation: Chen, L.; Deng, R.; Zha, J.; Gu, J.; Xia, T.; Chen, R. Research on Rotor Dynamic Characteristics of High Speed Aviation Piston Pump. *Lubricants* **2025**, *13*, 51. https://doi.org/10.3390/lubricants13020051

Copyright: © 2025 by the authors. Licensee MDPI, Basel, Switzerland. This article is an open access article distributed under the terms and conditions of the Creative Commons Attribution (CC BY) license (https://creativecommons.org/licenses/by/4.0/).

1. Introduction

Hydraulic systems play an important role in the field of modern industry and aviation, and their performance directly determines the stability and reliability of mechanical equipment [1]. As one of the core components of the hydraulic system, the performance of the piston pump plays a decisive role in the working efficiency and lifespan of the entire system [2–4]. Especially in high-speed aviation applications, the piston pump needs to maintain efficient and stable operation under extreme working conditions, which puts forward higher requirements for the dynamic performance of the piston pump [5].

The rotor system of the piston pump is subjected to complex loading scenarios during operation. Many scholars have conducted extensive research on loading calculations for piston pumps. Edge et al. [6] used the axial piston pump model constructed by the lumped parameter method to calculate the effect of oil inertia on the pressure of the piston chamber, which improved the accuracy of the calculation of the oil pressure in the chamber. Liu et al. [7] proposed a method for calculating the loading scenarios on the three main friction pairs of piston pumps, providing an important reference for the design of piston pumps. With the rapid development of computer technology, computer simulation software such as AMESim has also been widely used in load analysis of piston pumps [8–10]. With the continuous improvement of the rotational speed of the piston pump, its dynamic characteristics have increasingly become the focus of many scholars. Milind et al. [11] combined multi-body dynamics (MBD) and finite element (FE) methods to establish a dynamic and vibration behavior model of an axial piston pump, predicted the dynamic excitation force of the bearing and the control piston position, and compared with the experimental results. It was found that the two were in good agreement. Hesheng et al. [12] established a dynamic model for the rotor–bearing system of an axial piston pump, and conducted both simulation and experimental analysis on the vibration response of the system to misalignment-friction mixed faults under different parameters. The results showed that the rotor speed, tilt dislocation, friction gap and friction stiffness have a significant impact on the vibration characteristics of the system, and the friction fault is dominant in the mixed fault. Song et al. [13] established the dynamic equilibrium equation of the axial piston pump, analyzed the dynamic loading transfer path between the pump rotor and the shell, and discussed the influence of these loading scenarios on the dynamic response of the shell. Hu [14] established a lumped parameter model for the rotor system based on rotor dynamics theory and calculated the critical speed of the bearing–rotor system in the axial piston pump using the finite element method.

In the existing research, the load analysis of the piston pump rotor system generally adopts the method of independent calculation of the swash plate load and the valve plate load [15–17]. Specifically, firstly, the swash plate load on the plunger is determined by force balance analysis; secondly, according to the principle of fluid dynamics, the load of the valve plate is calculated separately. Finally, these two loads are combined and applied to the piston pump rotor system. It is worth noting that the cylinder and the spindle are connected by splines, which cannot transmit the axial force [18,19]. Since both the swash plate load and the valve plate load act on the cylinder block, and the two are independently calculated, the axial load of the cylinder block cannot be effectively balanced, and the deviation of the load calculation results is introduced. This deviation will make the dynamic characteristics analysis of the piston pump rotor system inaccurate, affecting the design and performance evaluation of the piston pump. Therefore, for the rotor system, starting from the overall force balance, the load at the swash plate and the valve plate is comprehensively calculated, and the interaction and transmission path of the force is more accurately revealed, which provides a new method for the dynamic analysis of the piston pump.

In this paper, the high-speed aviation piston pump is taken as the research object. Firstly, the kinematics and mechanics analysis of the piston is carried out in detail, and the contact force, friction force, and swash plate load of the piston cavity under various working conditions are calculated. Secondly, combined with the friction force of the plunger cavity, the force balance analysis is carried out to calculate the load of the valve plate, and the bearing load and its stiffness characteristics under different working conditions are further solved. Finally, based on the bearing stiffness parameters, the spindle dynamics model and the piston pump rotor system dynamics model are established, and the accuracy of the model is verified by ANSYS. In addition, in order to comprehensively evaluate the dynamic

characteristics of the piston pump, the transfer matrix method is used to analyze the critical speeds of the two models under different working conditions. In view of the shortcomings of the existing load calculation method of the piston pump, this study proposes a new load calculation method, which provides a new perspective for the in-depth study of the dynamic characteristics of the piston pump, helps to improve the stability and reliability of the piston pump, and provides a certain idea for the design improvement and technological innovation of the piston pump.

2. Modeling of Swash Plate Loading

The structure of the axial piston pump studied in this research is shown in Figure 1a. Its structure mainly includes spindle, front bearing, swash plate, slipper, cylinder block, chuck, piston, valve plate, and tail bearing, in which the swash plate and valve plate are rigidly connected to the shell. As shown in Figure 1b, the cylinder block, piston, slipper, and chuck rotate with the spindle during the working process, and all rotating parts together form the rotor system of the piston pump.

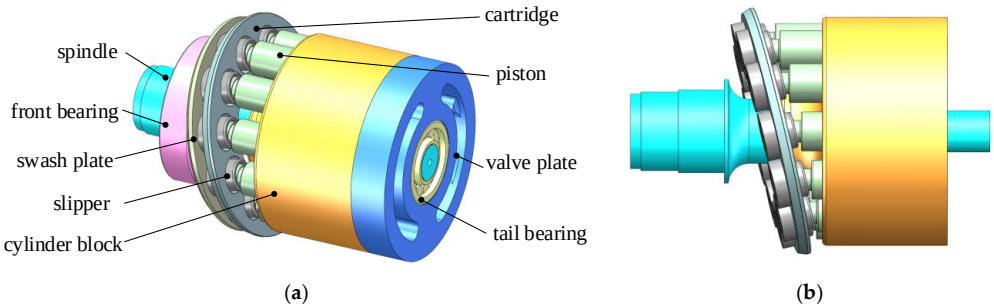


Figure 1. Structure of piston pump: (**a**) The structure of the axial piston pump; (**b**) the rotor system of the piston pump.

In the working process of the axial piston pump, the piston not only makes a circular motion with the cylinder but also makes a reciprocating linear motion relative to the cylinder under the action of the swash plate. The motion state of the piston is the superposition of two motions. Taking the axial direction of the piston pump as the z-axis, the positive direction of the z-axis is the direction of the swash plate pointing to the valve plate, the center of the swash plate is the coordinate origin O, and the positive direction of the y-axis is vertical upward, the global coordinate system xyz is established, as shown in Figure 2a. When the inclination angle of the swash plate of the piston pump is 0°, the pump has no flow output, but there is still a certain degree of leakage inside. In order to compensate for this leakage, the swash plate is designed to have a cross-angle, as shown in Figure 2b,c, where γ is the inclination angle of the swash plate, and β is the cross-angle of the swash plate.

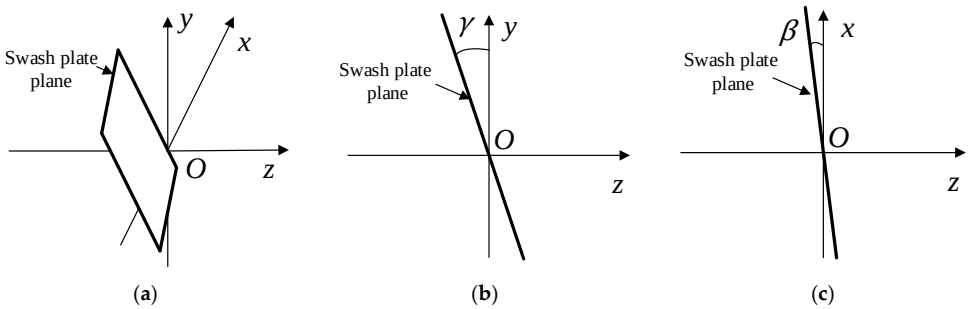


Figure 2. Coordinate system of piston pump: (**a**) The global coordinate system xyz; (**b**) the inclination angle of the swash plate; (**c**) the cross-angle of the swash plate.

2.1. Kinematic Modeling of the Piston

The kinematic analysis of the piston is shown in Figure 3. For a point M with a rotation angle of θ in the figure, its coordinate in the global coordinate system xyz is [20]:

$$\begin{aligned} x &= -R\sin\theta \\ y &= R\cos\theta \\ z &= -R(\tan\gamma\cos\theta - \tan\beta\sin\theta) \end{aligned} \tag{1}$$

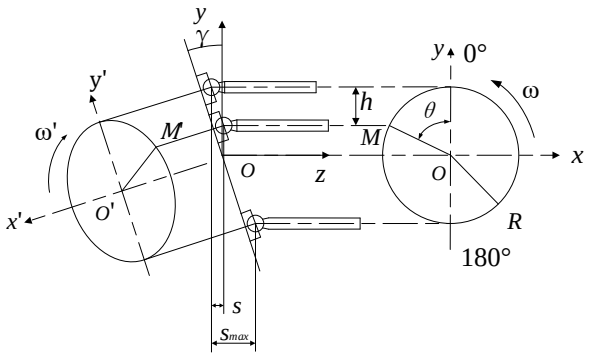


Figure 3. Kinematics analysis diagram of piston.

The position of the upper dead point (θ = 0°) is the displacement zero point of the reciprocating motion of the piston, and then the displacement s, velocity v, and acceleration a of the reciprocating motion of the piston are:

$$s = R(\tan\gamma(1-\cos\theta) + \tan\beta\sin\theta) \tag{2}$$

$$v = \frac{ds}{dt} = \frac{ds}{d\theta}\frac{d\theta}{dt} = R\omega(\tan\gamma\sin\theta + \tan\beta\cos\theta) \tag{3}$$

$$a = \frac{dv}{dt} = \frac{dv}{d\theta}\frac{d\theta}{dt} = R\omega^2(\tan\gamma\cos\theta - \tan\beta\sin\theta) \tag{4}$$

R is the radius of the piston distribution circle, and ω is the angular velocity of the piston pump rotation.

During the circular motion of the piston with the cylinder block, the piston also has centripetal acceleration a_r, which can be expressed as:

$$a_r = \omega^2 R \tag{5}$$

2.2. Reaction Force Analysis of the Piston

During the operation of the piston pump, the piston is simultaneously subjected to multiple forces such as hydraulic pressure, friction, inertial force, piston cavity contact force, and swash plate support reaction force. The force diagram is shown in Figure 4.

For the force of the piston, there is the force balance shown in Formula (6) and the moment balance equation shown in Formula (7) [21].

$$\begin{cases} \sum F_x = F_{rx} + F_{Nx} + F_{1x} + F_{2x} = 0 \\ \sum F_y = F_{ry} + F_{Ny} + F_{1y} + F_{2y} = 0 \\ \sum F_z = F_p + F_{Nz} + F_f + F_g = 0 \end{cases} \tag{6}$$

$$\begin{cases} \sum M_x = -F_{ry}\cdot l_a - F_{1y}\cdot(l-l_1) - F_{2y}\cdot l + \mathrm{sgn}(\sin\theta) f(F_{1y}+F_{2y})\cdot\frac{d}{2} = 0 \\ \sum M_y = F_{rx}\cdot l_a + F_{1x}\cdot(l-l_1) + F_{2x}\cdot l - \mathrm{sgn}(\sin\theta) f(F_{1x}+F_{2x})\cdot\frac{d}{2} = 0 \end{cases} \tag{7}$$

where l_a is the distance from the center of gravity of the piston to the center of the piston head; l_1 is the length of the piston in the piston cavity, and its calculation formula is:

$$l_1 = l - l_0 - R(\tan\gamma\cos\theta - \tan\beta\sin\theta) \tag{8}$$

where l is the length of the piston, l_0 is the distance between the center of the swash plate and the front surface of the cylinder block.

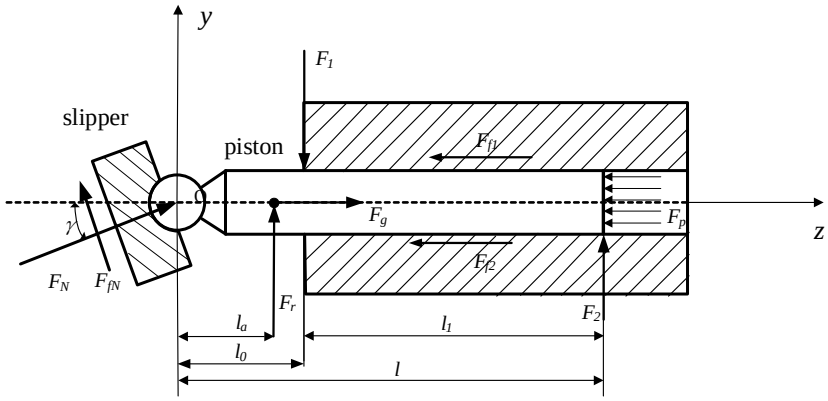


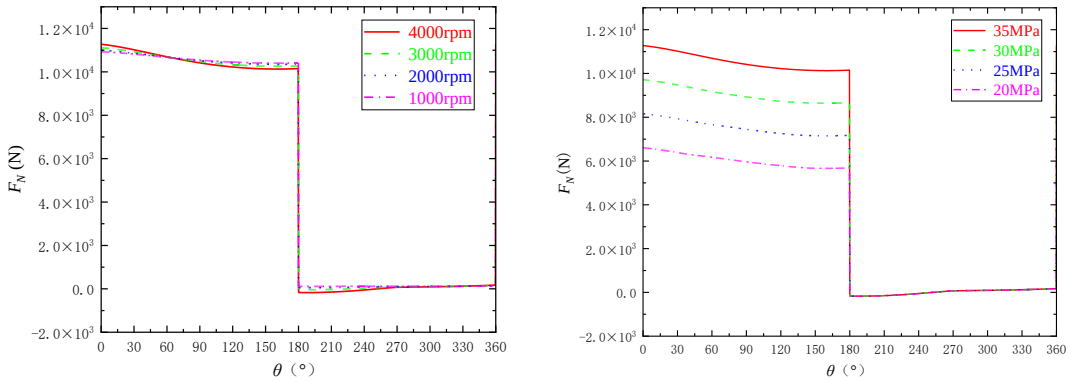
Figure 4. Force diagram of the piston.

2.3. Supporting Force of Swash Plate

Table 1 shows the working parameters of the piston pump and the structural parameters of the piston. Substituting each parameter into the Formulas (6) and (7), the swash plate support reaction force and the piston cavity contact force of the piston in a cycle can be solved. The calculation results differ under variable speed and variable outlet pressure. The swash plate support reaction force is shown in Figure 5a,b, and the calculation results of the piston cavity contact force under the rated working condition of 4000 rpm and 35 MPa are shown in Figure 6.

Table 1. Parameters of piston pump.

Parameters	Value	Parameters	Value	Parameters	Value
l	67.5 mm	β	4.2°	l_0	25 mm
R	41 mm	P_h	20/25/30/35 MPa	m	0.121 kg
γ	14.9°	P_l	0.45 MPa	f	0.1
n	1000/2000/3000/4000 rpm	d	18.8 mm		



(**a**) (**b**)

Figure 5. The reaction force of swash plate support under different working conditions: (**a**) Force of the swash plate reaction under variable speed (35 MPa); (**b**) force of the swash plate reaction under variable outlet pressure (4000 rpm).

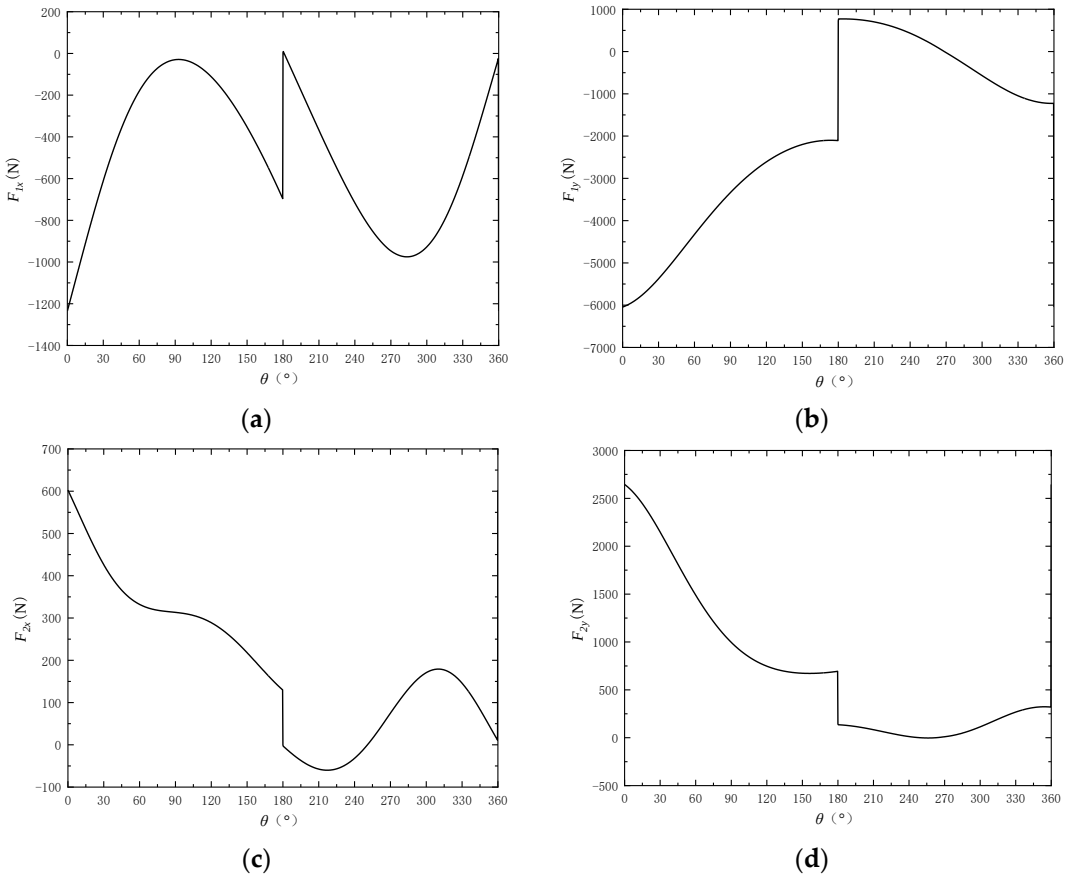


Figure 6. Contact force of piston cavity under rated working condition: (**a**) The piston cavity contact force of F_{1x}; (**b**) the piston cavity contact force of F_{1y}; (**c**) the piston cavity contact force of F_{2x}; (**d**) the piston cavity contact force of F_{2y}.

Comparing the swash plate reaction force under variable speed and variable outlet pressure, it is found that when the rotation angle is 0–180°, the speed has little effect on the swash plate reaction force, while the outlet pressure has a great influence on the swash plate reaction force. The greater the outlet pressure, the greater the swash plate reaction force. The reason is that when the rotation angle is 0–180°, the swash plate reaction force is mainly affected by the outlet pressure, and the inertial force has little effect on it. When the rotation angle is 180–270°, the influence of rotational speed on the reaction force of the swash plate is obvious. When the rotation angle is 180–270°, the inertia force of the piston is larger, and the influence of inertia force on the reaction force of the swash plate is greater than that of the outlet pressure.

2.4. Resulting Moment of Swash Plate

The reaction force of the swash plate of a single piston can be decomposed into three directions of x, y, and z in the global coordinate system, as shown in Formula (9), and the action point of the reaction force is shown in the global coordinate system as shown in Formula (10). Similarly, the swash plate reaction force of the remaining pistons and the coordinates of their action points can be calculated. The swash plate reaction force of the 11 pistons is concentrated and equivalent to the origin O of the global coordinate system. The resultant force and torque calculation after equivalence is shown in Formulas (11) and (12).

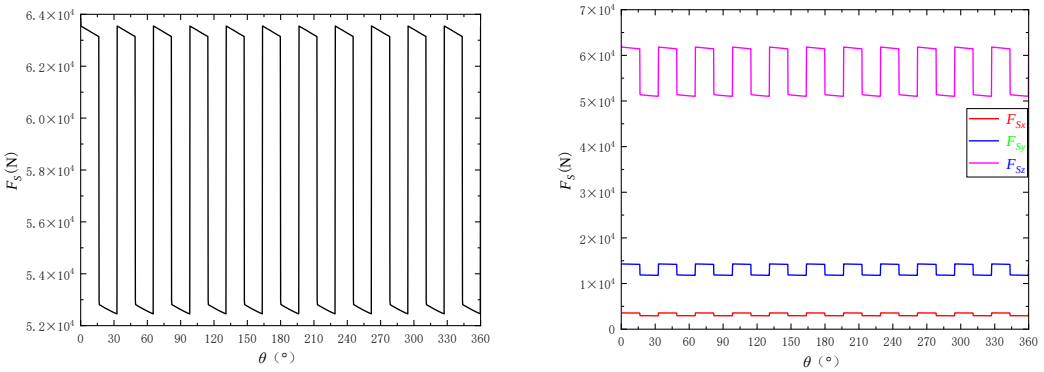
$$\vec{F}_N = [F_x, F_y, F_z] \tag{9}$$

$$\vec{r} = [x, y, z] = [-R\sin\theta, R\cos\theta, -R(\tan\gamma\cos\theta - \tan\beta\sin\theta)] \tag{10}$$

$$\vec{F}_S = \sum_{i=1}^{11} \vec{F}_{Ni} = [\sum_{i=1}^{11} F_{xi}, \sum_{i=1}^{11} F_{yi}, \sum_{i=1}^{11} F_{zi}] \tag{11}$$

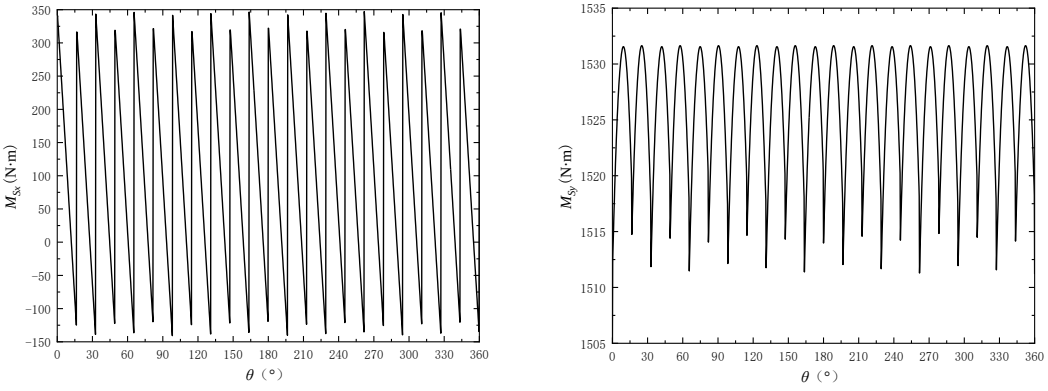
$$\vec{M}_S = \sum_{i=1}^{11} \vec{M}_{Ni} = [\sum_{i=1}^{11} M_{Nxi}, \sum_{i=1}^{11} M_{Nyi}, \sum_{i=1}^{11} M_{Nzi}] = \sum_{i=1}^{11} \vec{r}_i \times \vec{F}_{Ni} \tag{12}$$

The calculation results of the reaction force of the swash plate support are shown in Figure 7a, and the component forces of each axis are shown in Figure 7b. Because the component force of the reaction force of the swash plate support in the z-axis direction is balanced with the hydraulic pressure and friction force at the tail of the piston, the component force in the z-axis direction is much larger than that in the other two directions. The inclination angle of the swash plate is greater than the transverse angle, so the force in the y-axis direction is greater than the force in the x-axis direction. The calculation results of the equivalent x-axis torque of the swash plate are shown in Figure 8a, and the equivalent y-axis torque is shown in Figure 8b. Because the y-axis is the dividing line between the high-pressure zone and the low-pressure zone of the piston pump, the reaction force of the swash plate on both sides of the y-axis is quite different, so the equivalent y-axis torque is much larger than the equivalent x-axis torque.



(**a**) (**b**)

Figure 7. The counterforce of swash plate support under rated working conditions: (**a**) Support reaction force; (**b**) component force in each axis.



(**a**) (**b**)

Figure 8. Equivalent torque of swash plate under rated condition: (**a**) x-axis torque; (**b**) y-axis torque.

3. Bearing Stiffness Modeling

3.1. Modeling of Valve Plate Loading

The connection structure between the cylinder block and the main shaft is shown in Figure 9. Since the cylinder block and the main shaft are connected by a drum spline, the

main shaft at the spline has no axial force on the cylinder block. There is an axially arranged compression spring between the main shaft and the cylinder block. The direction of the spring compression force is shown in Figure 9. In addition, the cylinder block is subjected to the friction force of each piston cavity, the hydraulic compression force at the bottom of the piston cavity, and the reaction force of the valve plate. The axial balance equation is shown in Equation (13).

$$\sum F_{zq} = \sum_{i=1}^{11} F_{fi} + F_{plp} + F_k + \sum_{i=1}^{11} F_{bi} = 0 \tag{13}$$

where F_{fi} is the friction force of the i th piston on the cylinder block, F_{plp} is the reaction force of the valve plate, F_k is the spring compression force, and its F_{bi} is the friction force of the i th piston on the cylinder block.

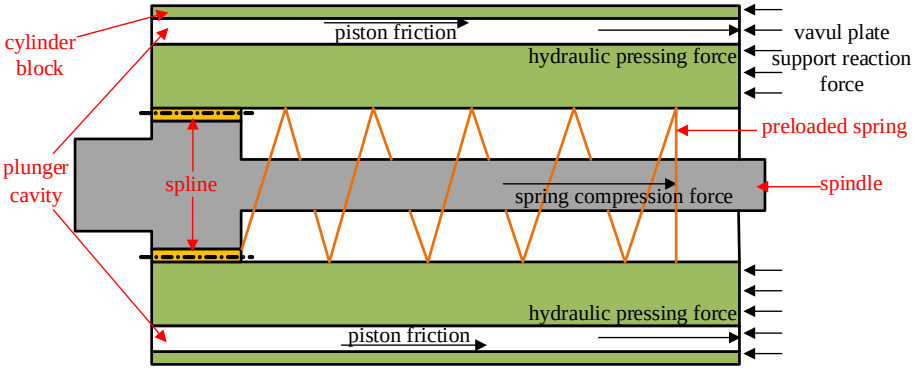


Figure 9. Force diagram of cylinder block.

Due to the complexity of the pressure distribution of the valve plate in the working process, it is difficult to calculate the reaction force directly. Therefore, the hydraulic uniform loading at the valve plate is equivalent to the concentrated loading on each piston cavity. The force diagram of the piston chamber is shown in Figure 10, and the equilibrium equation of each piston chamber is shown in Equation (15). The support reaction force of the valve plate of the piston chamber at variable speed is solved, and the support reaction force of the valve plate of each piston chamber is concentrated and equivalent to the origin O of the global coordinate system. The calculation results of the equivalent x-axis torque of the valve plate under rated conditions are shown in Figure 11a, and the calculation results of the equivalent y-axis torque are shown in Figure 11b. Similar to the equivalent torque of the swash plate side, the equivalent y-axis torque of the valve plate side is much larger than the equivalent x-axis torque.

$$F_{bi} = \begin{cases} \frac{\pi}{4} d^2 P_h & (0 \le \theta_i < \pi) \\ \frac{\pi}{4} d^2 P_l & (\pi \le \theta_i < 2\pi) \end{cases} \tag{14}$$

$$\sum F_{zsqi} = F_{fi} + F_{plpi} + F_{ki} + F_{bi} = 0 \tag{15}$$

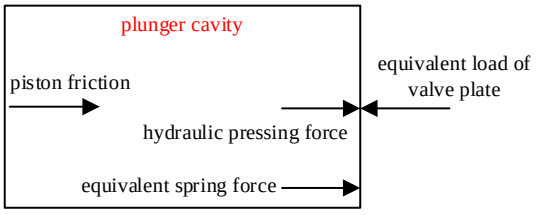
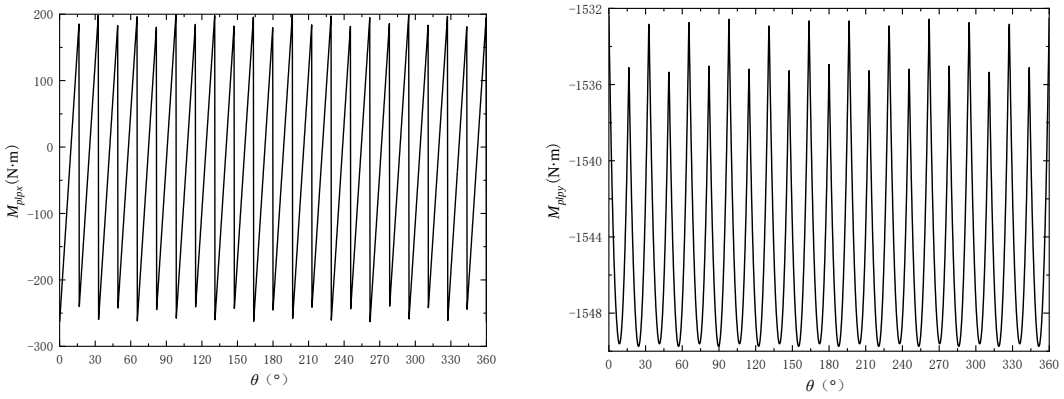


Figure 10. The force diagram of the piston cavity.

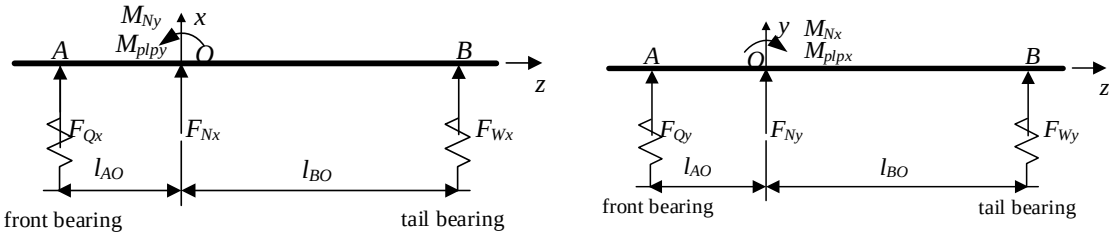


(**a**) (**b**)

Figure 11. Equivalent torque of valve plate under rated condition: (**a**) *x*-axis torque; (**b**) *y*-axis torque.

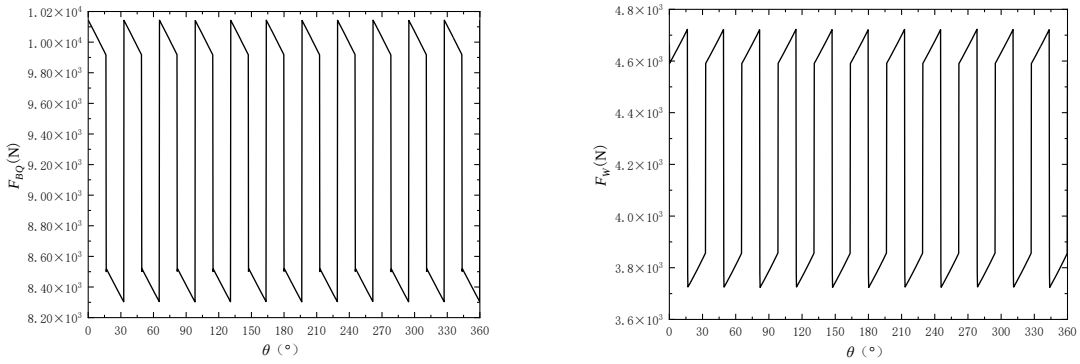
3.2. Reaction Force of Bearing

For the piston pump rotor system, the external force has the swash plate support reaction force, the valve plate support reaction force and the bearing support force. The *xoz* plane and *yoz* plane force diagram of the rotor system after the swash plate support reaction force and the valve plate support reaction force are concentrated, and the equivalent is shown in Figure 12. Under rated conditions, the calculation results of the front bearing support force are shown in Figure 13a, and the calculation results of the tail bearing support force are shown in Figure 13b. The front bearing support force is always greater than the tail bearing support force.



(**a**) (**b**)

Figure 12. Force diagram of rotor system: (**a**) Force of *xoz* plane; (**b**) Force of *yoz* plane.



(**a**) (**b**)

Figure 13. Force of bearing support under rated conditions: (**a**) Support force of front bearing; (**b**) support force of tail bearing.

Taking the average bearing support force in a cycle as the bearing load, the bearing load under variable speed is obtained as shown in Figure 14a. As the speed increases, the

bearing load of the front bearing becomes larger, and the bearing load of the tail bearing becomes smaller. The bearing load under variable outlet pressure is shown in Figure 14b. As the outlet pressure increases, both the front bearing and the tail bearing become larger.

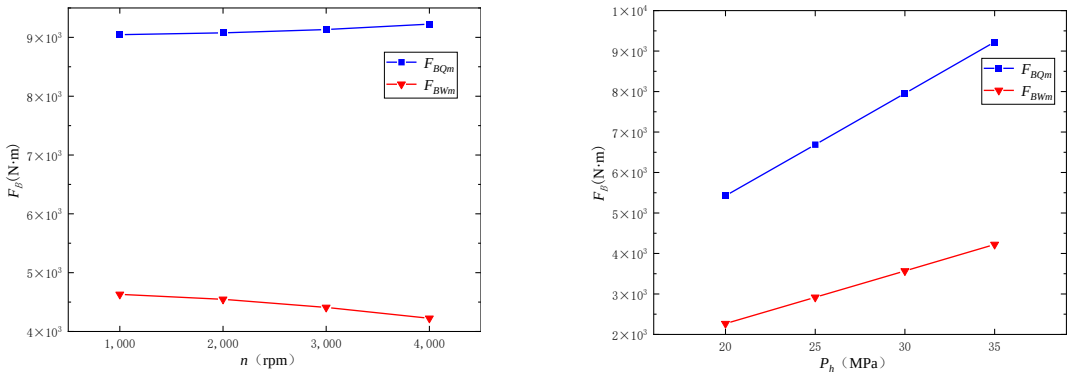


Figure 14. Bearing load: (**a**) Bearing load at variable speed; (**b**) bearing load variable outlet pressure.

3.3. Support Stiffness

The front bearing is an angular contact ball bearing. During the operation of the piston pump, it is not only affected by the radial force, but also by the axial preload force. The preload force is provided by the preload spring between the spindle and the cylinder body, and the size is 1000 N. It is assumed that the contact between the rolling element of the bearing and the inner and outer rings is elastic deformation, and the influence of operating temperature and other factors on the bearing is ignored. According to the method described in reference [22–24], the radial stiffness of the bearing under combined loading is calculated. The radial stiffness of the front bearing under variable speed and variable outlet pressure conditions is shown in Figure 15. With the increase in rotational speed and outlet pressure, the stiffness of the front bearing increases.

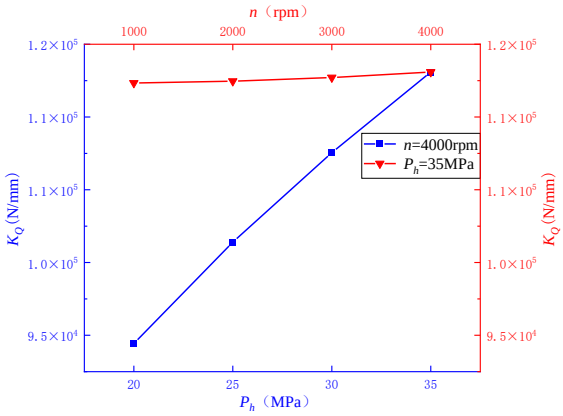


Figure 15. Stiffness of front bearing.

The tail bearing is a cylindrical roller bearing, which is only subjected to radial force during operation. Similar to the bearing condition of deep groove ball bearing only subjected to radial force, the calculation of radial support stiffness of needle roller bearing can be calculated by the stiffness calculation method of deep groove ball bearing only subjected to radial force in reference [25]. Because the rolling body of deep groove ball bearing is point contact with inner and outer rings, and the rolling body of needle roller

bearing is line contact with inner and outer rings, it is necessary to change the point Hertz contact formula in reference [25] to the line contact Hertz formula shown in Formula (16).

$$Q = K\delta^{10/9} \tag{16}$$

where Q is the radial load, δ is the displacement, K is the load displacement coefficient, which is related to the material and curvature radius of the inner and outer rings of the bearing.

The radial stiffness of the front bearing at variable speed is shown in Figure 16. As the speed increases, the bearing stiffness of the tail bearing becomes smaller. As the outlet pressure increases, the tail bearing stiffness becomes larger.

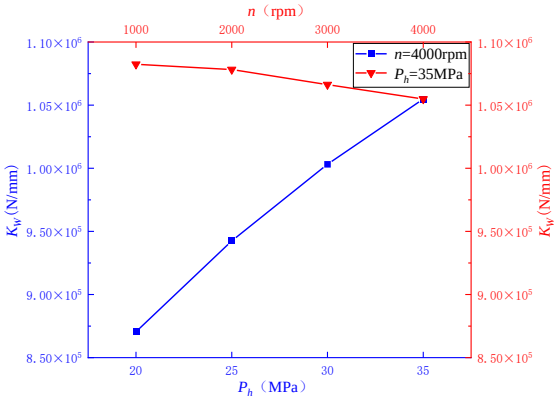


Figure 16. Stiffness of tail bearing.

Comparing the stiffness of the two bearings under the same working conditions, it is found that the stiffness of the tail bearing is much larger than that of the front bearing. It is speculated that the tail bearing is a needle roller bearing, and the linear contact stiffness between the needle roller and the inner and outer rings is much larger than the point contact stiffness between the ball roller and the inner and outer rings of the front bearing.

4. Critical Speed Analysis

Both the transfer matrix method and the finite element method can be used to calculate the critical speed of the rotor system. Although the finite element method has high calculation accuracy, it requires more computing resources, which is particularly difficult for the calculation of complex models. In contrast, the transfer matrix method is realized by numerical calculation, which has the advantage of fast calculation speed. However, when the transfer matrix method is applied, the model is partially simplified, which may have an impact on the final calculation results. In order to ensure the rationality of these simplifications, we use the finite element method for further verification.

4.1. Critical Speed of Spindle

4.1.1. Transfer Matrix Method

According to the principle of discrete equivalence, the spindle is equivalent to a discrete system composed of several shaft segments and supports. Through this treatment, the dynamic model of the spindle is simplified so that it can be used for subsequent critical speed calculation. The equivalent spindle model after discretization is shown in Figure 17, the shaft consists of 25 segments and 26 nodes, and the bearings are located at the 7th and 25th nodes.

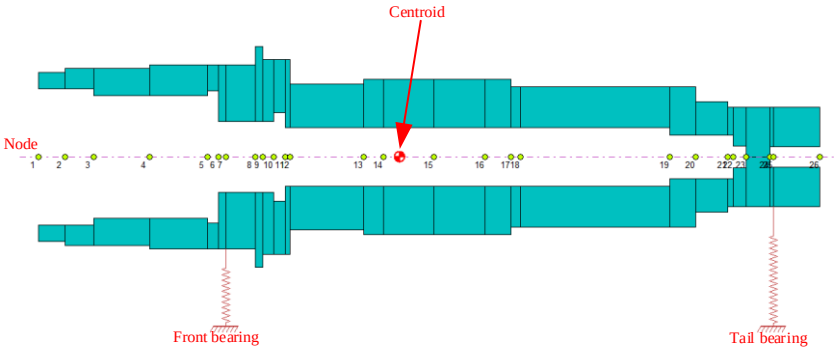


Figure 17. Discrete equivalent model of spindle.

The commercial dynamic analysis software Dyrobes (V20.20) [26] is used to simulate the discrete model of the spindle, and the bearing stiffness is set according to the theoretical calculation results in Section 2.3. The first four critical speeds of the spindle under variable speed and variable outlet pressure conditions are calculated as shown in Table 2. With the increase in rotational speed, the critical speed of each order of the spindle decreases, but the change is very small. As the outlet pressure increases, the first to fourth critical speeds of the spindle increase, and the first critical speed changes the most.

Table 2. Critical speed of each order of the spindle under variable conditions.

Working Condition	First Order/rpm	Second Order/rpm	Third Order/rpm	Fourth Order/rpm
1000 rpm–35 MPa	207,760	560,035	1,190,580	1,643,640
2000 rpm–35 MPa	207,725	559,788	1,190,020	1,643,570
3000 rpm–35 MPa	207,619	559,064	1,188,400	1,643,380
4000 rpm–35 MPa	207,519	558,359	1,186,870	1,643,200
4000 rpm–30 MPa	206,838	554,906	1,179,940	1,642,290
4000 rpm–25 MPa	205,977	550,405	1,172,110	1,641,270
4000 rpm–20 MPa	204,841	544,301	1,163,240	1,640,110

In order to deeply understand the vibration characteristics of the spindle, this study further analyzes its first–fourth order vibration mode and obtains the first–fourth order vibration mode of the spindle under rated conditions, as shown in Figure 18. The purple curve is the modal shape of the spindle.

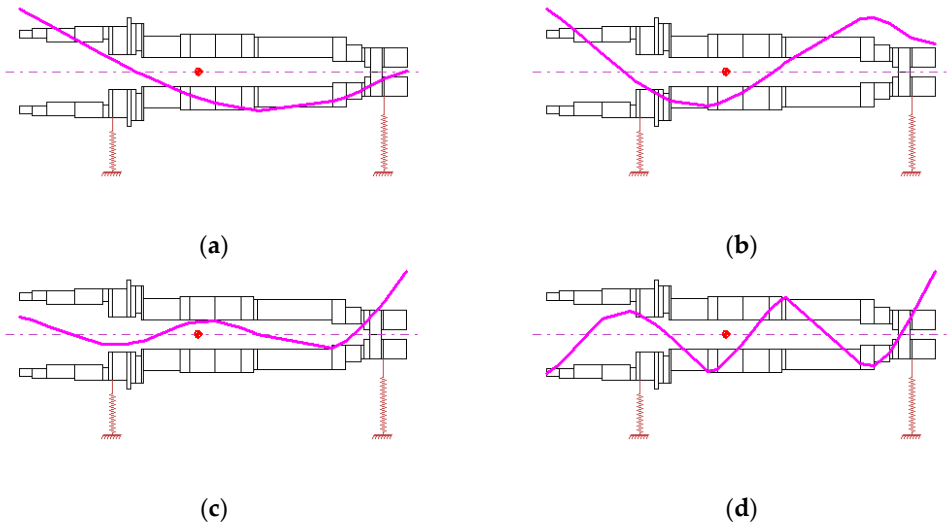


Figure 18. The modal vibration mode of the spindle under rated working condition: (**a**) First-order vibration mode; (**b**) second-order vibration mode; (**c**) third-order vibration mode; (**d**) fourth-order vibration mode.

4.1.2. Finite Element Method

In order to verify the accuracy of the transfer matrix method to calculate the critical speed of the spindle, the finite element method is used to analyze the modal of the spindle under rated conditions. Before the modal analysis, the spindle model must be meshed to ensure the accuracy and reliability of the analysis results. In order to truly reflect the support conditions of the bearing on the spindle, this study uses the bearing connection method to connect the spindle to the ground and uses the boundary condition setting method of remote displacement to set constraints at the spindle bearing position to limit the axial displacement of the spindle. At the same time, the spindle is allowed to vibrate freely in the direction perpendicular to the axis, ensuring that the modal analysis results can truly reflect the dynamic characteristics of the spindle in actual operation. The results of the first four-order modal shapes of the spindle under rated conditions calculated by Ansys are shown in Figure 19, and the first four-order critical speeds of the spindle under rated conditions compared with Ansys (V2022R1) and Dyrobes (V20.20) are shown in Table 3.

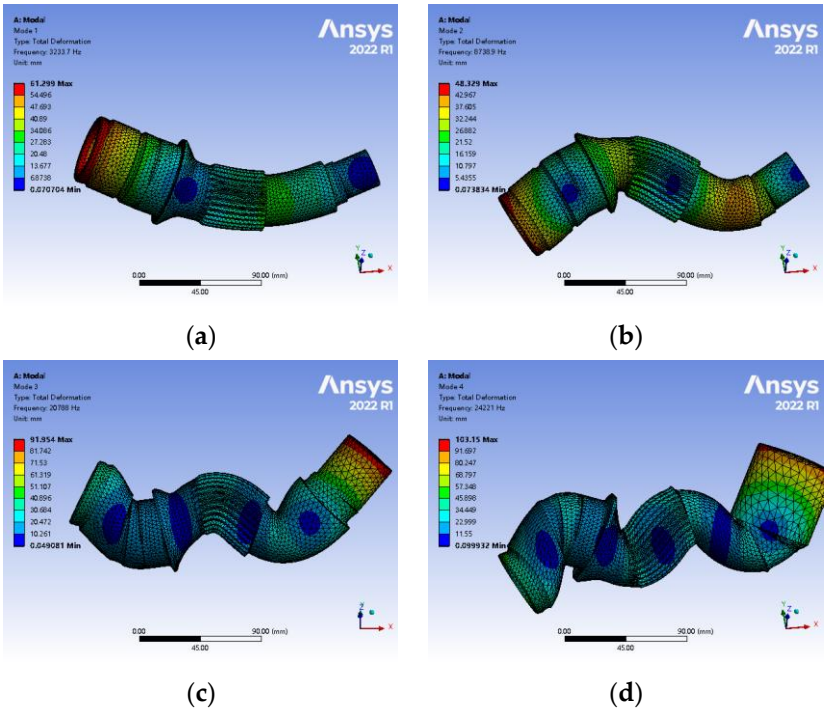


Figure 19. The modal vibration mode of spindle analyzed by Ansys: (**a**) First-order vibration mode; (**b**) second-order vibration mode; (**c**) third-order vibration mode; (**d**) fourth-order vibration mode.

Table 3. Comparison of critical speed of spindle under rated condition.

Order	Ansys/rpm	Dyrobes/rpm	Error/%
First order	194,022	207,519	3.36
Second order	524,334	558,359	3.14
Third order	1,247,280	1,186,870	2.48
Fourth order	1,453,260	1,643,200	6.13

Comparing Figures 18 and 19, it is found that the first–fourth-order vibration modes of the spindle calculated by the finite element method and the transfer matrix method are almost the same. Taking the mean value of the calculation results of Ansys and Dyrobes as the reference value, and it can be seen from Table 3 that the error of the critical speed calculated by the two methods is small, which verifies the accuracy of the transfer matrix method.

4.2. Critical Speed of Rotor System

In the dynamic analysis of the rotor system, in addition to considering the main shaft, it is necessary to include key rotating components such as chucks, slippers, pistons, and cylinder blocks. Because of their large mass and moment of inertia, these components play a vital role in the dynamic characteristics of the rotor system. In order to simplify the computational complexity, these rotating components are regarded as a whole and equivalent to disk elements for analysis. The rotating component and the spindle are connected by a drum spline, and the spline structure makes the meshing stiffness between the spindle and the rotating component rather than the rigid connection. In order to calculate the meshing stiffness of the spline pair, the finite element method is used to analyze and calculate the spline pair, and the meshing stiffness of the spline pair is 1.932×10^{10} N·mm/rad. The discrete equivalent model of the rotor system is obtained. As shown in Figure 20, the disk element and the spindle are connected by spline at the 15th node. The centroid is located at the 18th node, and the unbalance is applied to the centroid.

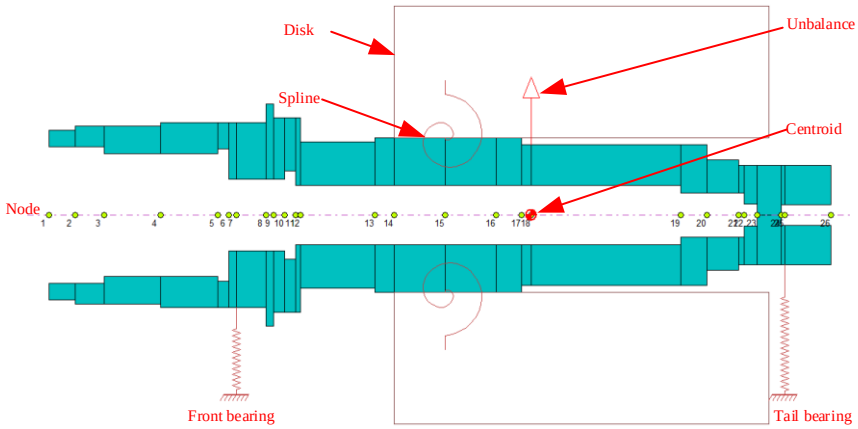


Figure 20. Discrete equivalent model of the rotor system.

The model and the meshing stiffness of the spline pair shown in Figure 20 are substituted into Dyrobes, and the first four critical speeds of the spindle under variable speed and variable outlet pressure conditions are calculated as shown in Table 4. As the speed increases, the first-order critical speed of the rotor system increases, and the third-to-sixth-order critical speed decreases, but the change range is very small. As the outlet pressure increases, the critical speeds of each order increase, but the change range is within 1%.

Table 4. Critical speed of each order of the rotor system under variable conditions.

Working Condition	First Order/rpm	Second Order/rpm	Third Order/rpm	Fourth Order/rpm
1000 rpm–35 MPa	53,215	551,776	1,030,340	1,572,850
2000 rpm–35 MPa	53,219	551,466	1,029,350	1,572,710
3000 rpm–35 MPa	53,222	550,558	1,026,480	1,572,300
4000 rpm–35 MPa	53,234	549,674	1,023,740	1,571,920
4000 rpm–30 MPa	52,765	545,428	1,011,190	1,570,180
4000 rpm–25 MPa	52,190	539,901	996,267	1,568,200
4000 rpm–20 MPa	51,458	532,459	978,334	1,565,940

Compared with the critical speed of the Table 2 spindle, after adding the disk unit, the critical speed of each order of the rotor system is smaller than that of the spindle, and the first-order critical speed decreases the most, but the first-order critical speed is still much larger than the rated speed.

In the first–fourth-order vibration mode of the rotor system under rated conditions, As shown in Figure 21, the purple curve is the modal shape of the rotor system, and the

blue dotted line is the position of the disk element under the modal shape. Compared with Figure 18, the modal shapes of each order are uniformly and greatly changed.

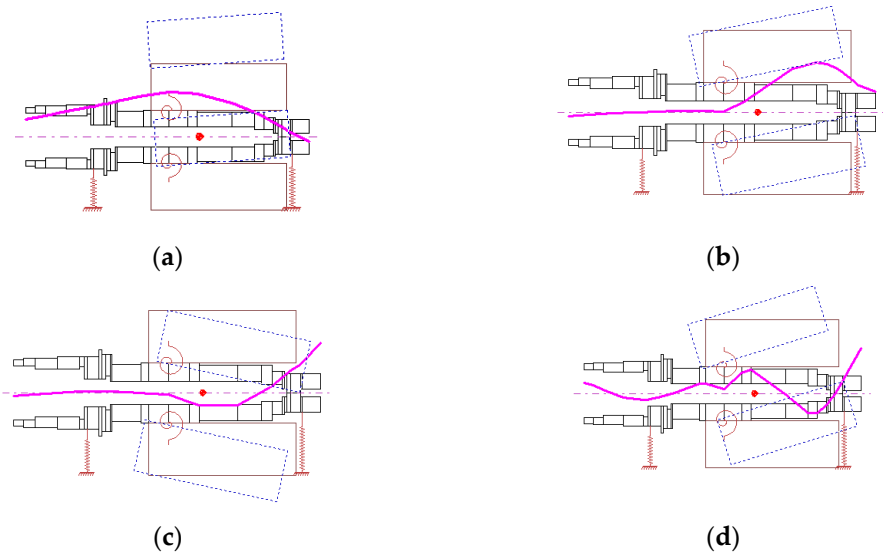


Figure 21. The modal vibration mode of the rotor system under rated working condition: (**a**) First-order vibration mode; (**b**) second-order vibration mode; (**c**) third-order vibration mode; (**d**) fourth-order vibration mode.

Similarly, Ansys is used to calculate the critical speed and modal shape of the rotor system under rated conditions. The calculation results are shown in Figure 22 and Table 5. The calculation results are similar, which verifies the accuracy of the discrete model of the rotor system.

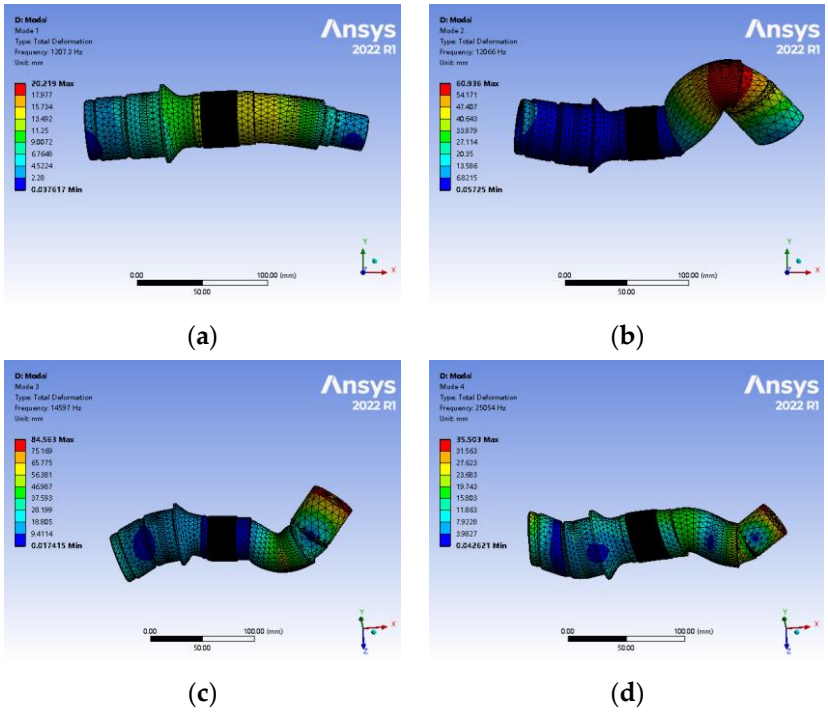


Figure 22. The modal vibration mode of rotor system analyzed by Ansys: (**a**) First-order vibration mode; (**b**) second-order vibration mode; (**c**) third-order vibration mode; (**d**) fourth-order vibration mode.

Table 5. Comparison of critical speed of rotor system under rated condition.

Order	Ansys/rpm	Dyrobes/rpm	Error/%
First order	72,438	53,234	15.28
Second order	723,960	549,674	13.68
Third order	875,820	1,023,740	7.79
Fourth order	1,503,240	1,571,920	2.23

The changes in rotational speed will lead to the change to the centrifugal force and inertia force of the plunger, which will affect the bearing stiffness and the load of the rotor system, thus changing the dynamic characteristics of the rotor system. However, since the variation in centrifugal force and inertial force is smaller than that of hydraulic pressure, the influence of rotational speed on the rotor system is relatively lower than that of outlet pressure. Although the critical speeds of each order of the rotor system under different working conditions change, the change range is very small, and the influence of working condition parameters on the critical speed can be ignored. The influence of rotating components on the rotor system is great, which will not only make the critical speed of each order of the rotor system decrease obviously, but also make the vibration mode change and change the weak parts under the vibration mode.

5. Conclusions

Based on the force of the piston pump, the force and bearing stiffness of the piston pump under variable working conditions were analyzed, as well as the dynamic characteristics of the high-speed aviation piston pump. The conclusions are as follows:

(1) Through the modeling of kinematics and force of the piston, the dynamic balance method is used to construct the mechanical balance equation of the piston, and the influence of the working condition parameters on the reaction force of the swash plate is revealed. The outlet pressure plays a leading role in the reaction force of the swash plate. The greater the outlet pressure, the greater the reaction force.

(2) The bearing load under each working condition is obtained, and the bearing stiffness under different working conditions is calculated by the quasi-static method. The stiffness of the front bearing increases and the stiffness of the tail bearing decreases with the increase of the rotational speed. As the outlet pressure increases, the stiffness of the front bearing and the tail bearing increases.

(3) The critical speed and modal shape of the spindle under rated working conditions are analyzed by the transfer matrix method and finite element method, respectively, and the accuracy of the discrete equivalent model is verified. The critical speed of the shaft under different working conditions is calculated by the transfer matrix method, where the working condition parameters have little effect on the critical speed.

(4) The key rotating components, such as the chuck, slipper, piston, and cylinder block, are equivalent to disk units, and the meshing stiffness of the spline is calculated by the finite element method. Substituting it into the discrete equivalent model, the critical speed of the rotor system is calculated. Considering the disk unit in the modeling, the weak parts of the modal shape changed, and the critical speed of the rotor system is obviously reduced, but it is still far exceeded the rated speed.

Although this paper has achieved some research results, the main result is to simplify the influence of the nonlinear characteristics of the friction pair on the dynamic behavior of the piston pump [27]. In addition, the calculation of bearing stiffness is based on a series of assumptions, which may lead to a certain deviation in the calculation results. In general, the results of this study provide a new perspective for the in-depth study of the load and dynamic characteristics of the piston pump, which is helpful in improving the stability and

reliability of the piston pump and provides some ideas for the design improvement and technological innovation of the piston pump. In future work, the bearing stiffness of the dynamic model will be corrected by the bearing stiffness test. The dynamic characteristics of the piston pump considering the nonlinearity of the friction pair are analyzed, and the corresponding experimental research is carried out.

Author Contributions: Conceptualization, L.C. and R.D.; methodology, L.C., R.D., J.Z. and J.G.; software, L.C. and R.D.; validation, J.Z., J.G., T.X. and R.C.; formal analysis, L.C.; investigation, R.D., J.Z., J.G., T.X. and R.C.; resources, L.C.; data curation, J.Z. and R.C.; writing—original draft preparation, R.D.; writing—review and editing, J.Z.; visualization, J.G.; supervision, T.X.; project administration, T.X.; funding acquisition, L.C. All authors have read and agreed to the published version of the manuscript.

Funding: This research received no external funding.

Data Availability Statement: Data are contained within the article.

Conflicts of Interest: The authors declare no conflicts of interest.

References

1. Liu, Y.-W.; Cheng, Y.-Q.; Wu, J.-J. Research progress of intelligent control methods in space propulsion systems. *Acta Aeronaut. Astronaut. Sin.* **2023**, *44*, 195–214. [CrossRef]
2. Wang, Q.; Wang, H.-H.; Yuan, S.; Wang, J.; Lin, N.-M.; Liu, Z.-Q.; Zeng, Q.-F.; Wu, Y.-C. Research Progress on Service Damage and Protection of Slipper-swashplate Pairs of Axial Piston Pump. *Surf. Technol.* **2023**, *52*, 126–139. [CrossRef]
3. Liu, J.; Liu, B.; Wu, X.; Du, P.-X.; Yang, Y.-L. Research on oil film lubrication and structural optimization of the mating pair of axial piston pumps. *Mach. Tool Hydraul.* **2024**, *52*, 213–221. [CrossRef]
4. Du, Z.-L.; Zhang, Y.-M. A time-varying reliability-based robust design method considering overall efficiency of axial piston pump. *Proc. Inst. Mech. Eng. Part O J. Risk Reliab.* **2022**, *236*, 936–954. [CrossRef]
5. Hu, M.; Gao, P.; Min, S.-J.; Liu, R.; Qiu, T.-X.; Zeng, Y.-S.; Liu, C.-H. Study on the Solid-liquid Interaction Characteristics of the Oil Film within Piston Cylinder Pair of the Ultra-high Pressure Swash Plate Type Axial Piston Pump. *J. Mech. Eng.* **2022**, *58*, 438–452. [CrossRef]
6. Edge, K.A.; Darling, J. The Pumping Dynamics of Swash Plate Piston Pumps. *J. Dyn. Syst. Meas. Control* **1989**, *111*, 307–312. [CrossRef]
7. Liu, Y.-S.; Li, Z.-Y. *Hydraulic Components and Systems*; Mechanical Industry Press: Beijing, China, 2019; pp. 80–97.
8. Milind, T.R.; Mitra, M. A Study on the Flexible Multibody Dynamic Modeling of an Axial Piston Pump Considering Housing Flexibility. *Procedia Eng.* **2016**, *144*, 1234–1241. [CrossRef]
9. Yang, F.-Y.; Yang, J.; Wang, P.-Y.; Liu, X.-Y. The impact of piston angle on piston load. *Chin. Hydraul. Pneum.* **2012**, *36*, 44–46. [CrossRef]
10. Zhang, Z.-F. Simulation of CY Axial Piston Pump And Optimization of Cylinder Structure. Master's Thesis, Inner Mongolia University of Science & Technology, Inner Mongolia, China, 2019. [CrossRef]
11. Milind, T.R.; Mitra, M. A Study on the Dynamics and Vibration Behavior of an Axial Piston Pump Using Combined MBD/FE Approach. *Procedia Eng.* **2016**, *144*, 452–460. [CrossRef]
12. Tang, H.-S.; Ren, Y.; Xiang, J.-W.; Kuma, A. Numerical and experimental analysis of rotor-bearing system for axial piston pump with misalignment–rubbing coupling fault. *J. Sound Vib.* **2023**, *559*, 117786. [CrossRef]
13. Song, H.-Q.; Wang, T.; Wang, H.-J. Dynamic characteristic analysis of housing for a swash-plate axial piston pump. *J. Vib. Shock* **2023**, *42*, 175–180+195. [CrossRef]
14. Hu, L.-H. Dynamic Analysis of Bearing Rotor System of Hydraulic Axial Piston Pump. *Mach. Tool Hydraul.* **2020**, *48*, 189–192. [CrossRef]
15. Ye, S.-G.; Zhang, J.-H.; Xu, B.; Zhu, S.Q.; Xiang, J.-W.; Tang, H.-S. Theoretical Investigation of the Contributions of the Excitation Forces to the Vibration of an Axial Piston Pump. *Mech. Syst. Signal Process.* **2019**, *129*, 201–217. [CrossRef]
16. Ran, Q.-P. Dynamic Characteristic Analysis and Structure Optimization of Swash-Plate Axial Piston Pump Shell. Master's Thesis, Shanghai Jiao Tong University, Shanghai, China, 2021. [CrossRef]
17. Haidak, G.; Wang, D.; Shiju, E. Research on the Thermo-Elastic Deformation and Fracture Mechanism of the Slipper Retainer in the Axial Piston Pumps and Motors. *Eng. Fail. Anal.* **2019**, *100*, 259–272. [CrossRef]
18. Li, Y.-J.; Zhao, G.; Wu, X.-S.; Li, J.; Yuan, W.; Mei, Q. Review of research on self-excited vibration of aviation spline-rotor system. *Acta Aeronaut. Astronaut. Sin.* **2022**, *08*, 21–35. [CrossRef]

19. Huang, W.-K.; Tian, H.-X.; Ma, H.; Wang, P.-F.; Yang, Y.; Han, Q.-K. An improved method for calculating the lateral and angular stiffness of spline couplings considering parallel misalignment. *Mech. Mach. Theory* **2023**, *189*, 105436. [CrossRef]
20. Xu, B.; Ye, S.-G.; Zhang, J.-H.; Zhang, C.-F. Flow ripple reduction of an axial piston pump by a combination of cross-angle and pressure relief grooves: Analysis and optimization. *J. Mech. Sci. Technol.* **2016**, *30*, 2531–2545. [CrossRef]
21. Ran, Q.-P.; Wang, T.; Liu, B.; Dong, X.-J. Dynamic Characteristic Analysis for Rotor System of Swash-plate Axial Piston Pump. *Chin. Hydraul. Pneum.* **2021**, *45*, 134–142. [CrossRef]
22. Chen, R.-L.; Zhao, S.-D.; Zhang, M.-H.; Zhang, Y.-C.; Cui, Y.-H. Time-varying Stiffness Model and Load-bearing Characteristics Analysis of Angular Contact Ball Bearings. *Mach. Des. Res.* **2022**, *38*, 114–119. [CrossRef]
23. Zhu, C.-F.; Yang, D.-F.; Zhang, Z.-Q.; Gou, H. Numerical and Experimental Study on Dynamic Characteristics of Angular Contact Ball Bearing. In *Manufacturing Technology & Machine Tool*; Delmar Publishers: Clifton Park, NY, USA, 2015; pp. 83–88. [CrossRef]
24. Fang, B.; Zhang, L.; Qu, X.-T.; Zhao, J. Theoretical and experimental research of stiffness of angular contact ball bearing. *J. Jilin Univ. (Eng. Technol. Ed.)* **2012**, *42*, 840–844. [CrossRef]
25. Chen, R.-L.; Han, Q.; Zhang, M.-H.; Zhang, Y.-C.; Li, L.-L.; Cui, Y.-H. Stiffness Model of Rolling Bearing Considering Clearance and Analysis of Its Time-varying Characteristic. *J. Mech. Transm.* **2021**, *45*, 8–14. [CrossRef]
26. Becze, S.; Vuscan, I.G. Comparison study regarding bearing performance on 3 types of air bearings using Dyrobes software. *MATEC Web Conf.* **2019**, *299*, 04001. [CrossRef]
27. Ying, P.-T.; Tang, H.-S.; Chen, L.; Ren, Y.; Kuma, A. Dynamic Modeling and Vibration Characteristics of Multibody System in Axial Piston Pump. *Alex. Eng. J.* **2022**, *62*, 523–540. [CrossRef]

Disclaimer/Publisher's Note: The statements, opinions and data contained in all publications are solely those of the individual author(s) and contributor(s) and not of MDPI and/or the editor(s). MDPI and/or the editor(s) disclaim responsibility for any injury to people or property resulting from any ideas, methods, instructions or products referred to in the content.